Published by
NIGERIAN SOCIETY OF PHYSICAL SCIENCES
Available online @ https://journal.nsps.org.ng/index.php/jnsps

J. Nig. Soc. Phys. Sci. 8 (2026) 3028

Journal of the Nigerian Society of Physical Sciences

Velocity-in/dependent double folding analysis of ^{12}C + ^{12}C elastic scattering cross section at different energies

Sunday D. Olorunfunmi[a,*], Armand Bahini[b], Samuel A. Adeojo[a]

[a]*Department of Physics & Engineering Physics, Obafemi Awolowo University, Ile-Ife, 220005, Osun State, Nigeria*
[b]*Université de Caen Normandie, ENSICAEN, CNRS/IN2P3, LPC Caen UMR6534, F-14000 Caen, France*

Abstract

This study investigates the elastic scattering cross sections for ^{12}C + ^{12}C over a wide range of incident energies from 78.85 to 420 MeV using the velocity–dependent São Paulo Potential version 2 (SPP2) and the velocity–independent Brazilian Nuclear Potential (BNP) within the optical-model-based double folding (DF) framework. Two different density distributions for ^{12}C, experimental matter density (ED), and the Dirac-Hartree-Bogoliubov (DHB) theoretical matter density, were employed. The analysis compares the computed potentials, obtained by folding the density distributions, and evaluates the accuracy of the results through comparison with experimental data. Two approaches were explored to determine the depths of the potentials, highlighting their performance and sensitivity to energy and density distributions. Results indicate good agreement with experimental data, with SPP2 generally outperforming BNP. Analysis of volume integrals and reaction cross sections further elucidates the behavior of the potentials and their implications on scattering phenomena. Overall, this study provides insights into the dynamics of nuclear interactions at intermediate energies, contributing to the understanding of nuclear reactions.

DOI:10.46481/jnsps.2026.3028

Keywords: Velocity–dependent potential, Double folding model, Cross section, São Paulo potential

Article History :
Received: 23 June 2025
Received in revised form: 19 August 2025
Accepted for publication: 13 October 2025
Available online: 27 January 2026

Communicated by: B. J. Falaye

1. Introduction

In the realm of heavy ion (HI) scattering, understanding the intricate interplay of nuclear forces and dynamics has been a subject of extensive investigation over the past three decades. Numerous efforts have been dedicated to formulating folding models of the optical model potential, particularly for analyzing elastic and inelastic scattering phenomena involving heavy ions [1–7]. The foundational double folding (DF) model, rooted in a realistic effective nucleon-nucleon (NN) interaction [8], initially proved successful in describing scattering reactions primarily governed by strong absorption, wherein the elastic scattering data of HI became sensitive solely to the surface characteristics of the nucleus-nucleus potential.

However, the efficacy of the simple DF model was questioned in cases where refractive or rainbow scattering phenomena were observed, indicating a broader sensitivity of the data to the nuclear potential across a wider radial domain. This limitation prompted further exploration, with various investigations discussing the refractive scattering contributions in HI systems such as ^{12}C+^{12}C, ^{12}C+^{16}O, and ^{16}O+^{16}O [5, 6, 9–12].

Efforts to enhance the predictive power of the folding models led to the development of variants such as the density-dependent M3Y effective NN interaction [13], termed DDM3Y, aimed at effectively accounting for in-medium effects, particu-

*Corresponding author Tel. No.: +234-904-271-3841.
Email address: sundayolorunfunmi@gmail.com (Sunday D. Olorunfunmi)

larly significant at inter-nuclear distances [2–6]. Subsequent analyses employed different density-dependent versions of the M3Y interaction for studying the elastic scattering data of systems like ^{12}C+^{12}C and ^{16}O+^{16}O [5, 6] .

Recent studies have underscored the importance of incorporating rearrangement effects and energy dependence into the nuclear mean-field potential within the double folding framework [14, 15]. For instance, Khoa *et al.* [14] utilized an extended double-folding model with density-dependent CDM3Yn interactions to investigate the elastic scattering of ^{12}C+^{12}C, particularly at refractive energies, revealing noticeable impacts of the rearrangement term on the nucleus-nucleus optical potential, particularly at small inter-nuclear distances.

Furthermore, Mahmoud and Hassanien [16] conducted a comprehensive reanalysis of the refractive scattering phenomenon in ^{12}C+^{12}C over a broad energy spectrum, employing optical-model-based folded potentials rooted in the Jeukenne–Lejeune–Mahaux (JLM) effective NN interaction. Their findings highlighted the ability of the real JLM folded potentials, complemented by shallow Woods-Saxon (WS) imaginary potentials, to systematically reproduce the general features of refractive elastic scattering in the ^{12}C+^{12}C system.

Also, in another study, Hassanain *et al.* [17] investigated the ^{12}C+^{12}C system using the double folding cluster (DFC) optical potential based on the 3α Nucleon and N-N effective interactions. The generated potentials reproduced well the elastic scattering reaction cross section of all the experimental data in the 70 – 360 MeV energy range considered.

Motivated by these advancements and the ongoing quest for improved predictive capabilities in heavy ion scattering, this study aims to conduct an optical-model-based double folding analysis of ^{12}C+^{12}C elastic scattering cross-sections at various energies. In particular, we will employ the recently proposed velocity-dependent São Paulo Potential version 2 (SPP2) and the velocity-independent Brazilian Nuclear Potential (BNP) by Chamon *et al.* [18]. These potentials, which have recently found application in scattering studies involving stable and unstable nuclei [19–26], will be evaluated for their suitability in describing heavy ion reactions, with a focus on the ^{12}C+^{12}C system.

The structure of this paper is outlined as follows: Section 2 provides a concise overview of the theoretical formalism. The methodology employed for calculations is elaborated upon in Section 3. Section 4 is dedicated to presenting the results and engaging in discussions thereof. Finally, Section 5 encapsulates the conclusions drawn from this study.

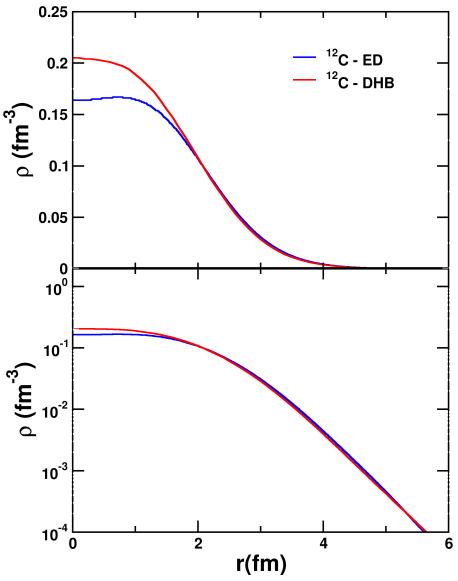

Figure 1: Experimental (ED) and Dirac-Hartree-Bogoliubov (DHB) nuclear densities of ^{12}C used in the present work.

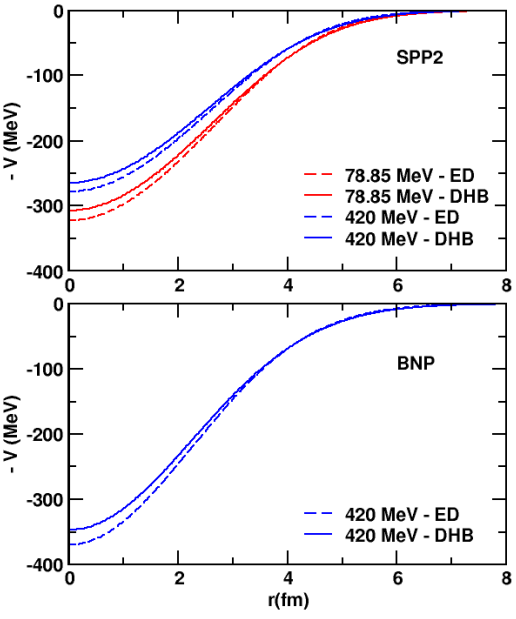

Figure 2: Real folded ^{12}C + ^{12}C potentials with SPP2 and BNP interactions using ED and DHB densities at 78.85 and 420 MeV.

2. Formalism

The analysis of elastic scattering cross sections within the optical model entails solving the Schrodinger equation utilizing a conventional complex optical potential given by:

$$U_{\rm opt}(r) = V(r) + iW(r), \tag{1}$$

where $V(r)$ and $W(r)$ denote the real and imaginary components, respectively. In microscopic model analysis, one or both components of the optical potential are frequently derived from the double folding model, expressed as:

$$V_F(R) = \int \rho_1(r_1)\rho_2(r_2)v_{nn}(R - r_1 - r_2)dr_1dr_2, \tag{2}$$

where v_{nn} represents the effective nuclear interaction, ρ_1 signifies the density of the projectile, and ρ_2 stands for the density of the target nucleus. This investigation explores two distinct forms of effective nuclear interactions, specifically the SPP2 and BNP interactions. The effective nuclear interactions pro-

posed by Chammon *et al.* [18, 27, 28] for the SPP2 and BNP potentials are briefly outlined here. A detailed explanation of this formalism is available in Ref. [18, 27, 28] and the associated literature.

The velocity-dependent SPP2 effective nuclear interaction is parameterized as follows [18]:

$$v_{nn}^{\mathrm{SPP2}}(r) = -U_0 \exp^{-(r/a)^2} \exp^{-\frac{4v^2}{c^2}}, \tag{3}$$

with $U_0 = 735.813$ MeV, $a = 0.5$ fm, c denotes the speed of light, and v represents the relative velocity between the interacting nuclei. The velocity is related to the incident energy $E_{\mathrm{c.m.}}$, kinetic energy E_k, and the reduced mass μ of the system, given by [18]:

$$v^2(R, E_{\mathrm{c.m.}}) = c^2 - \left(\frac{\mu c^3}{\mu c^2 + E_k}\right)^2. \tag{4}$$

As per Refs. [18, 27, 28], the BNP effective nuclear interaction is velocity-independent and is expressed as:

$$v_{nn}^{\mathrm{BNP}}(r) = -U_0 \exp^{-(r/a)^2}, \tag{5}$$

with $U_0 = 87.226$ MeV and $a = 0.95$ fm.

3. Method of calculation

In this study, the potentials and cross sections calculations were performed using the REGINA computer code [18]. Both the experimental matter density (ED) [29] and the Dirac-Hartree-Bogoliubov (DHB) [30] theoretical nuclear density calculated through the DHB model were implemented in the REGINA code to account for different density distributions of ^{12}C.

To construct the total optical potential, two distinct approaches were adopted. In the first approach, the real potential was constructed using the double-folding model (DFM), with the normalization factor fixed at 1. Meanwhile, the imaginary potential was allowed to vary to achieve the best fit with the experimental data. In this regard, two cases were considered. At first, the imaginary potential is taken to be of Woods-Saxon (WS) form, and the optical potential $U_{\mathrm{opt}}(r)$ is expressed as:

$$U_{\mathrm{opt}}(r) = N_R V_F(r) + i \frac{-W_{\mathrm{I}}}{1 + \exp\left(\frac{r - r_{\mathrm{I}}\left(A_{\mathrm{P}}^{1/3} + A_{\mathrm{T}}^{1/3}\right)}{a_{\mathrm{I}}}\right)}, \tag{6}$$

where W_{I}, a_{I}, and r_{I} represent the depth, diffuseness, and reduced radius, respectively. The parameters a_{I} and r_{I} were fixed at 0.69 and 1.15 fm, respectively, while W_{I} was adjusted to achieve optimal agreement with the experimental data. The fixed values of a_I and r_I were determined through a systematic trial procedure: first, an initial guess for r_I was chosen and varied in steps of 0.1 fm while keeping a_I and W_I fixed; next, a_I was varied in steps of 0.01 fm while r_I and W_I were held constant. After a large number of such iterative calculations, convergence was achieved at $r_I = 1.15$ fm and $a_I = 0.69$ fm. Finally, the depth W_I of the imaginary potential was adjusted to obtain the best fit to the experimental scattering data. This

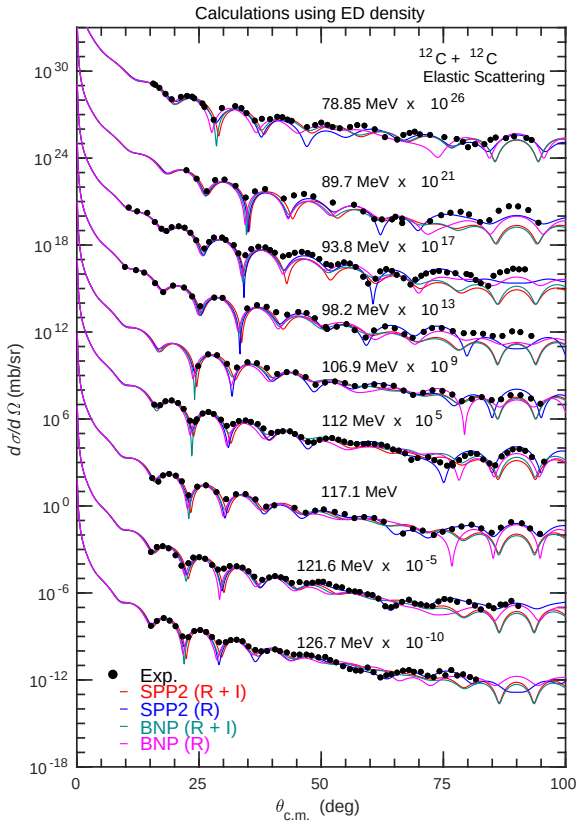

Figure 3: The angular distribution of ^{12}C + ^{12}C elastic scattering cross sections calculated using SPP2(R+I), SPP2(R), BNP(R+I) and BNP(R) potentials with ED density at 78.85, 89.7, 93.8, 98.2, 106.9, 112, 117.1, 121.6, and 126.7 MeV. Experimental data are taken from Ref. [31].

potential configuration is denoted as SPP2(R) and BNP(R) for SPP2 and BNP effective interactions, respectively. The second case is when the imaginary part is constructed from the normalized DF potential, and the optical potential is expressed as:

$$U_{\mathrm{opt}}(r) = (N_R + iN_I)V_F(r), \tag{7}$$

where N_R is the fixed normalization factor for the real potential (set to 1), and N_I is the normalization factor for the imaginary potential, which is allowed to vary to optimize the fit with experimental data. This configuration is labeled as SPP2(R+I) for SPP2 interaction and BNP(R+I) for BNP interaction.

The second approach involved a similar methodology as the second case described above, where both the real and imaginary potentials were constructed from the DFM, and both normalization factors N_R and N_I were adjusted to enhance the agreement with experimental data.

We conduct a search for the optimal renormalization factors and phenomenological potential parameters to minimize the χ^2

Table 1: The renormalization parameters (N_R and N_I) , imaginary WS parameters (W_I, r_I, a_I), the volume integrals (J_R and J_I), the total reaction cross sections σ_R and the χ^2/N values of $^{12}C+^{12}C$ elastic scattering at fourteen different incident energies using SPP(R+I), SPP2(R), BNP(R+I) and BNP(R) potentials with ED density of ^{12}C. The last column shows the χ^2/N values reported in Refs. [5, 17] for comparison.

Energy (MeV)	Potential	N_R	N_I	W_I (MeV)	r_I (fm)	a_I (fm)	J_R (MeVfm^3)	J_I (MeVfm^3)	σ_R (mb)	χ^2/N	χ^2/N[5, 17]
78.85	SPP2(R+I)	1.00	0.4	-	-	-	413.05	162.55	1252	16.96	28.3[17]
	SPP2(R)	1.00	-	13	1.15	0.69	413.05	64.49	1363	14.31	
	BNP(R+I)	1.00	0.4	-	-	-	416.43	166.57	1289	13.34	
	BNP(R)	1.00	-	14	1.15	0.69	416.43	69.45	1389	14.75	
89.7	SPP2(R+I)	1.00	0.7	-	-	-	410.41	287.29	1346	30.98	53.2[17]
	SPP2(R)	1.00	-	16	1.15	0.69	410.41	79.37	1415	20.75	
	BNP(R+I)	1.00	0.7	-	-	-	416.43	291.50	1392	31.17	
	BNP(R)	1.00	-	18	1.15	0.69	416.43	89.30	1452	31.22	
93.8	SPP2(R+I)	1.00	0.8	-	-	-	409.46	327.57	1373	17.48	
	SPP2(R)	1.00	-	16	1.15	0.69	409.46	79.37	1417	11.97	
	BNP(R+I)	1.00	0.7	-	-	-	416.43	291.50	1394	15.94	
	BNP(R)	1.00	-	18	1.15	0.69	416.43	89.30	1454	16.09	
98.2	SPP2(R+I)	1.00	0.7	-	-	-	408.47	285.93	1349	17.60	
	SPP2(R)	1.00	-	16	1.15	0.69	408.47	79.37	1418	12.00	
	BNP(R+I)	1.00	0.7	-	-	-	416.43	291.50	1396	17.88	
	BNP(R)	1.00	-	18	1.15	0.69	416.43	89.30	1455	15.34	
106.9	SPP2(R+I)	1.00	0.6	-	-	-	406.45	243.87	1322	12.50	10.3[17]
	SPP2(R)	1.00	-	17	1.15	0.69	406.45	84.33	1433	14.21	
	BNP(R+I)	1.00	0.6	-	-	-	416.43	249.86	1368	11.29	
	BNP(R)	1.00	-	18	1.15	0.69	416.43	89.30	1456	15.67	
112	SPP2(R+I)	1.00	0.7	-	-	-	405.23	283.66	1350	11.70	11.0[17]
	SPP2(R)	1.00	-	17.5	1.15	0.69	405.23	86.82	1440	8.04	13.5[5]
	BNP(R+I)	1.00	0.6	-	-	-	416.43	249.89	1368	15.87	
	BNP(R)	1.00	-	19.5	1.15	0.69	416.43	96.74	1475	16.06	
117.1	SPP2(R+I)	1.00	0.8	-	-	-	404.05	323.24	1375	25.07	12.3[17]
	SPP2(R)	1.00	-	18.5	1.15	0.69	404.05	91.78	1453	18.87	
	BNP(R+I)	1.00	0.7	-	-	-	416.43	291.50	1399	25.01	
	BNP(R)	1.00	-	20	1.15	0.69	416.43	99.22	1481	30.21	
121.6	SPP2(R+I)	1.00	0.8	-	-	-	403.01	322.41	1375	25.32	15.2[17]
	SPP2(R)	1.00	-	19.5	1.15	0.69	403.01	96.74	1466	10.78	
	BNP(R+I)	1.00	0.8	-	-	-	416.43	333.14	1427	15.14	
	BNP(R)	1.00	-	23	1.15	0.69	416.43	114.10	1517	17.96	
126.7	SPP2(R+I)	1.00	0.75	-	-	-	401.84	301.38	1361	8.82	12.4[17]
	SPP2(R)	1.00	-	20.5	1.15	0.69	401.84	101.70	1478	7.11	9.3[5]
	BNP(R+I)	1.00	0.75	-	-	-	416.43	312.32	1413	8.82	
	BNP(R)	1.00	-	21.5	1.15	0.69	416.43	106.66	1498	13.22	
180	SPP2(R+I)	1.00	0.85	-	-	-	389.87	331.39	1366	0.98	
	SPP2(R)	1.00	-	17.5	1.15	0.69	389.87	86.81	1415	1.93	
	BNP(R+I)	1.00	0.7	-	-	-	416.43	290.80	1383	3.72	
	BNP(R)	1.00	-	17	1.15	0.69	416.43	84.33	1416	5.10	
240	SPP2(R+I)	1.00	1.2	-	-	-	376.93	452.32	1416	37.56	42.2[5]
	SPP2(R)	1.00	-	28	1.15	0.69	376.93	138.90	1522	43.29	
	BNP(R+I)	1.00	1.1	-	-	-	416.43	458.07	1470	43.76	
	BNP(R)	1.00	-	30	1.15	0.69	416.43	148.83	1550	51.52	
300	SPP2(R+I)	1.00	0.8	-	-	-	364.53	291.62	1291	6.35	22.8[17]
	SPP2(R)	1.00	-	15	1.15	0.69	364.53	74.41	1309	4.12	23.2[5]
	BNP(R+I)	1.00	0.6	-	-	-	416.43	249.86	1301	3.88	
	BNP(R)	1.00	-	15	1.15	0.69	416.43	74.41	1319	3.80	
360	SPP2(R+I)	1.00	0.9	-	-	-	352.65	317.38	1289	14.26	13.2[17]
	SPP2(R)	1.00	-	25.5	1.15	0.69	352.65	126.50	1417	25.23	
	BNP(R+I)	1.00	0.9	-	-	-	416.43	374.79	1379	29.45	
	BNP(R)	1.00	-	28	1.15	0.69	416.43	138.90	1479	57.54	
420	SPP2(R+I)	1.00	0.9	-	-	-	341.25	307.13	1261	9.74	
	SPP2(R)	1.00	-	20	1.15	0.69	341.25	99.22	1341	11.62	
	BNP(R+I)	1.00	0.65	-	-	-	416.43	270.68	1279	11.80	
	BNP(R)	1.00	-	20	1.15	0.69	416.43	99.22	1351	17.82	

statistic, as defined by Eq. (1) [1]:

$$\chi^2 = \frac{1}{N}\sum_{k=1}^{N}\left[\frac{\sigma_{cal}(\theta_k) - \sigma_{ex}(\theta_k)}{\Delta\sigma_{ex}(\theta_k)}\right]^2. \quad (8)$$

Here, $\sigma_{cal}(\theta_k)$ and $\sigma_{ex}(\theta_k)$ represent the calculated and experimental cross sections, respectively, $\Delta\sigma_{ex}(\theta_k)$ denotes the experimental error, and N signifies the number of data points. For all considered data, we adopt an average experimental error of 10%.

The real (J_R) and imaginary (J_I) volume integrals are com-

Table 2: The renormalization parameters (N_R and N_I) , imaginary WS parameters (W_I, r_I, a_I), the volume integrals (J_R and J_I), the total reaction cross sections σ_R and the χ^2/N values of $^{12}C+^{12}C$ elastic scattering at fourteen different incident energies using SPP(R+I), SPP2(R), BNP(R+I) and BNP(R) potentials with DHB density of ^{12}C. The last column shows the χ^2/N values reported in Refs. [5, 17] for comparison.

Energy (MeV)	Potential	N_R	N_I	W_I (MeV)	r_I (fm)	a_I (fm)	J_R (MeVfm^3)	J_I (MeVfm^3)	σ_R (mb)	χ^2/N	χ^2/N[5, 17]
78.85	SPP2(R+I)	1.00	0.4	-	-	-	417.73	167.09	1336	12.17	28.3[17]
	SPP2(R)	1.00	-	14.5	1.15	0.69	417.73	71.92	1417	15.84	
	BNP(R+I)	1.00	0.4	-	-	-	416.43	166.57	1366	11.91	
	BNP(R)	1.00	-	14.5	1.15	0.69	416.43	71.92	1424	13.49	
89.7	SPP2(R+I)	1.00	0.65	-	-	-	415.08	269.8	1421	31.05	53.2[17]
	SPP2(R)	1.00	-	22	1.15	0.69	415.08	109.14	1513	33.26	
	BNP(R+I)	1.00	0.7	-	-	-	416.43	291.5	1476	32.67	
	BNP(R)	1.00	-	22	1.15	0.69	416.42	109.14	1520	30.66	
93.8	SPP2(R+I)	1.00	0.6	-	-	-	414.12	248.47	1408	16.38	
	SPP2(R)	1.00	-	19	1.15	0.69	414.12	94.26	1481	17.51	
	BNP(R+I)	1.00	0.6	-	-	-	416.43	249.86	1447	18.48	
	BNP(R)	1.00	-	19	1.15	0.69	416.43	94.26	1488	14.55	
98.2	SPP2(R+I)	1.00	0.7	-	-	-	413.1	289.17	1438	20.07	
	SPP2(R)	1.00	-	20	1.15	0.69	413.1	99.22	1494	21.39	
	BNP(R+I)	1.00	0.7	-	-	-	416.43	291.5	1480	22.95	
	BNP(R)	1.00	-	20	1.15	0.69	416.43	99.22	1500	20.33	
106.9	SPP2(R+I)	1.00	0.55	-	-	-	411.01	226.05	1392	22.88	10.3[17]
	SPP2(R)	1.00	-	19.5	1.15	0.69	411.01	96.74	1482	33.82	
	BNP(R+I)	1.00	0.55	-	-	-	416.43	229.04	1431	39.59	
	BNP(R)	1.00	-	20	1.15	0.69	416.43	99.22	1501	42.83	
112	SPP2(R+I)	1.00	0.6	-	-	-	409.75	245.85	1407	15.67	11.0[17]
	SPP2(R)	1.00	-	19.5	1.15	0.69	409.75	96.74	1487	23.94	13.5[5]
	BNP(R+I)	1.00	0.6	-	-	-	416.43	249.89	1449	22.76	
	BNP(R)	1.00	-	20	1.15	0.69	416.43	99.22	1500	16.59	
117.1	SPP2(R+I)	1.00	0.7	-	-	-	408.55	285.98	1437	30.34	12.3[17]
	SPP2(R)	1.00	-	23	1.15	0.69	408.55	114.1	1527	37.96	
	BNP(R+I)	1.00	0.7	-	-	-	416.43	291.5	1481	35.67	
	BNP(R)	1.00	-	20	1.15	0.69	416.43	99.22	1499	34.56	
121.6	SPP2(R+I)	1.00	0.8	-	-	-	407.48	325.98	1464	14.48	15.2[17]
	SPP2(R)	1.00	-	23	1.15	0.69	407.48	114.1	1527	12.95	
	BNP(R+I)	1.00	0.8	-	-	-	416.43	333.14	1511	16.14	
	BNP(R)	1.00	-	23	1.15	0.69	416.43	114.1	1533	9.4	
126.7	SPP2(R+I)	1.00	0.7	-	-	-	406.29	284.4	1434	11.46	12.4[17]
	SPP2(R)	1.00	-	22.5	1.15	0.69	406.29	111.62	1520	12.32	9.3[5]
	BNP(R+I)	1.00	0.7	-	-	-	416.43	284.4	1480	12.98	
	BNP(R)	1.00	-	22.5	1.15	0.69	416.43	111.62	1526	11.42	
180	SPP2(R+I)	1.00	0.4	-	-	-	394.04	157.62	1290	6.57	
	SPP2(R)	1.00	-	14	1.15	0.69	394.04	69.45	1372	9.67	
	BNP(R+I)	1.00	0.5	-	-	-	416.43	208.21	1384	20.29	
	BNP(R)	1.00	-	14	1.15	0.69	416.43	69.45	1379	28.49	
240	SPP2(R+I)	1.00	1	-	-	-	380.81	380.81	1460	44.12	42.2[5]
	SPP2(R)	1.00	-	30	1.15	0.69	380.81	148.83	1552	52.95	
	BNP(R+I)	1.00	1	-	-	-	416.43	416.43	1531	61.88	
	BNP(R)	1.00	-	32	1.15	0.69	416.43	158.75	1578	66.13	
300	SPP2(R+I)	1.00	0.6	-	-	-	368.14	220.88	1303	3.93	22.8[17]
	SPP2(R)	1.00	-	15.5	1.15	0.69	368.14	76.89	1327	4.87	23.2[5]
	BNP(R+I)	1.00	0.6	-	-	-	416.43	249.86	1375	16.46	
	BNP(R)	1.00	-	18.5	1.15	0.69	416.43	91.78	1389	20.04	
360	SPP2(R+I)	1.00	0.85	-	-	-	356	302.6	1357	22.85	13.2[17]
	SPP2(R)	1.00	-	26.5	1.15	0.69	356	131.46	1461	13.64	
	BNP(R+I)	1.00	0.8	-	-	-	416.43	333.14	1427	61.5	
	BNP(R)	1.00	-	30	1.15	0.69	416.43	148.83	1507	77.44	
420	SPP2(R+I)	1.00	0.7	-	-	-	344.39	241.07	1277	10.16	
	SPP2(R)	1.00	-	18.5.00	1.15	0.69	344.39	91.78	1322	13.86	
	BNP(R+I)	1.00	0.6	-	-	-	416.43	249.86	1329	24.86	
	BNP(R)	1.00	-	20	1.15	0.69	416.43	99.22	1480	32.63	

puted using the expressions:

$$J_R(E) = \frac{4\pi}{A_P A_T} \int V(r,E) r^2 dr, \tag{9}$$

$$J_I(E) = \frac{4\pi}{A_P A_T} \int W(r,E) r^2 dr, \tag{10}$$

where A_P and A_T denote the mass numbers of the projectile and target, respectively.

Table 3: The renormalization parameters (N_R and N_I) , the volume integrals (J_R and J_I), the total reaction cross sections σ_R and the χ^2/N values of $^{12}C+^{12}C$ elastic scattering at fourteen different incident energies using SPP(R+I) and BNP(R+I) potentials with ES and DHB densities of ^{12}C. The last column shows the χ^2/N values reported in Refs. [5, 17] for comparison.

Energy (MeV)	Density	Potential	N_R	N_I	J_R (MeVfm^3)	J_I (MeVfm^3)	σ_R (mb)	χ^2/N	χ^2/N[5, 17]
78.85	ED	SPP2(R+I)	1.50	0.40	619.575	165.22	1364	11.03	28.3[17]
		BNP(R+I)	1.50	0.40	624.645	166.572	1407	12.02	
	DHB	SPP2(R+I)	1.10	0.40	459.503	167.092	1364	11.49	
		BNP(R+I)	1.05	0.40	437.2515	166.572	1382	11.77	
89.7	ED	SPP2(R+I)	1.05	0.68	430.9305	283.1724	1354	30.93	53.2[17]
		BNP(R+I)	1.05	0.68	437.2515	283.1724	1401	30.83	
	DHB	SPP2(R+I)	0.95	0.65	394.326	269.802	1406	30.43	
		BNP(R+I)	0.90	0.65	374.787	270.6795	1429	30.85	
93.8	ED	SPP2(R+I)	1.20	0.70	491.352	286.622	1398	13.52	
		BNP(R+I)	1.10	0.65	458.073	270.6795	1408	14.62	
	DHB	SPP2(R+I)	0.95	0.70	393.414	289.884	1422	16.10	
		BNP(R+I)	0.90	0.60	374.787	249.858	1414	16.71	
98.2	ED	SPP2(R+I)	1.10	0.68	449.317	277.7596	1370	16.30	
		BNP(R+I)	0.99	0.68	412.2657	283.1724	1388	17.68	
	DHB	SPP2(R+I)	0.80	0.70	330.48	289.17	1373	18.98	
		BNP(R+I)	0.80	0.70	333.144	291.501	1411	20.26	
106.9	ED	SPP2(R+I)	1.10	0.60	447.095	243.87	1348	10.74	10.3[17]
		BNP(R+I)	1.02	0.58	424.7586	241.5294	1367	10.85	
	DHB	SPP2(R+I)	0.80	0.55	328.808	226.0555	1327	12.08	
		BNP(R+I)	0.80	0.55	333.144	229.0365	1362	11.73	
112	ED	SPP2(R+I)	1.01	0.68	409.2823	275.5564	1347	11.71	11.0[17]
		BNP(R+I)	0.95	0.68	395.6085	283.1724	1378	11.91	13.5[5]
	DHB	SPP2(R+I)	0.80	0.60	327.8	245.85	1342	12.27	
		BNP(R+I)	0.80	0.60	333.144	249.858	1379	11.22	
117.1	ED	SPP2(R+I)	0.95	0.75	383.8475	303.0375	1349	23.73	12.3[17]
		BNP(R+I)	0.95	0.75	395.6085	312.3225	1398	24.31	
	DHB	SPP2(R+I)	0.70	0.70	285.985	285.985	1333	22.01	
		BNP(R+I)	0.70	0.70	291.501	291.501	1371	23.65	
121.6	ED	SPP2(R+I)	1.20	0.90	483.612	362.709	1450	17.56	15.2[17]
		BNP(R+I)	1.05	0.80	437.2515	333.144	1441	14.58	
	DHB	SPP2(R+I)	0.90	0.80	366.732	325.984	1433	14.01	
		BNP(R+I)	0.80	0.80	333.144	333.144	1442	15.15	
126.7	ED	SPP2(R+I)	0.99	0.75	397.8216	301.38	1358	8.81	12.4[17]
		BNP(R+I)	0.90	0.75	374.787	312.3225	1382	8.04	9.3[5]
	DHB	SPP2(R+I)	0.80	0.70	325.032	284.403	1369	6.86	
		BNP(R+I)	0.75	0.70	312.3225	291.501	1391	7.83	
180	ED	SPP2(R+I)	0.97	0.89	378.1739	346.9843	1368	0.96	
		BNP(R+I)	0.90	0.80	374.787	333.144	1383	1.79	
	DHB	SPP2(R+I)	0.90	0.40	354.636	157.616	1258	4.92	
		BNP(R+I)	0.80	0.40	333.144	166.572	1263	3.70	
240	ED	SPP2(R+I)	0.95	1.20	358.0835	452.316	1402	36.91	42.2[5]
		BNP(R+I)	0.95	1.10	395.6085	458.073	1455	39.08	
	DHB	SPP2(R+I)	0.80	0.90	304.648	342.729	1369	30.13	
		BNP(R+I)	0.80	0.90	333.144	374.787	1433	30.49	
300	ED	SPP2(R+I)	1.05	0.70	382.7565	255.171	1275	5.66	22.8[17]
		BNP(R+I)	0.95	0.60	395.6085	249.858	1286	3.56	23.2[5]
	DHB	SPP2(R+I)	0.90	0.60	331.326	220.884	1272	3.40	
		BNP(R+I)	0.80	0.60	333.144	249.858	1304	3.63	
360	ED	SPP2(R+I)	1.05	0.95	370.2825	335.0175	1315	15.92	13.2[17]
		BNP(R+I)	0.90	0.90	374.787	374.787	1348	24.24	
	DHB	SPP2(R+I)	0.80	0.85	284.8	302.6	1291	6.21	
		BNP(R+I)	0.70	0.80	291.501	333.144	1316	6.41	
420	ED	SPP2(R+I)	1.01	0.80	344.6625	273	1246	8.88	
		BNP(R+I)	0.90	0.65	374.787	270.6795	1248	8.52	
	DHB	SPP2(R+I)	0.80	0.70	275.512	241.073	1212	7.41	
		BNP(R+I)	0.70	0.60	291.501	249.858	1218	6.85	

4. Results and discussion

4.1. General observations

The elastic scattering cross sections for ^{12}C + ^{12}C at inci-

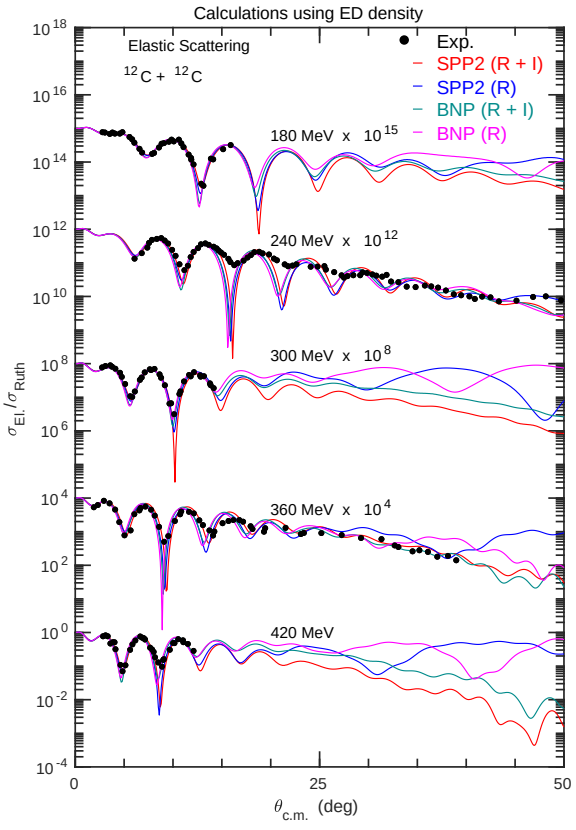

Figure 4: Ratio of elastic scattering to Rutherford cross section for $^{12}C + ^{12}C$ reaction calculated using SPP2(R+I), SPP2(R), BNP(R+I) and BNP(R) potentials with ED density at 180, 240, 300, 360, and 420 MeV. Experimental data are taken from Ref. [32].

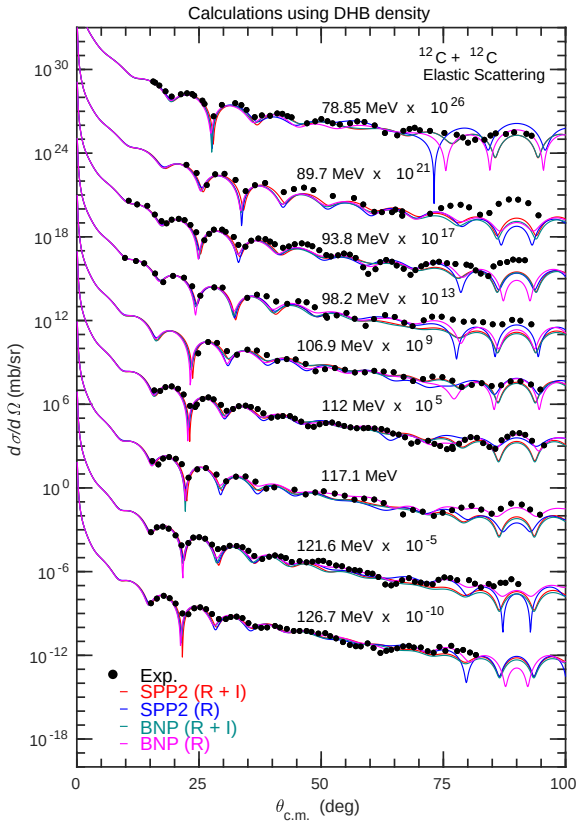

Figure 5: Same as Figure 3, but with the DHB density at 78.85, 89.7, 93.8, 98.2, 106.9, 112, 117.1, 121.6, and 126.7 MeV. Experimental data are taken from Ref. [31].

using the velocity-dependent SPP2 and velocity-independent BNP within the framework of DF optical model. The calculations involved two different matter density distributions for ^{12}C: ED and DHB densities. The corresponding folding optical potentials, denoted as V_F^{SPP2} and V_F^{BNP}, were computed according to the procedure outlined in Section 2, using Eqs. (2) – (5). Subsequently, the total optical potentials (OP) were constructed based on Eqs. (6) and (7).

Figure 1 compares the density distributions on linear and logarithmic scales. In the nuclear interior, the DHB calculation yields a higher central density than the ED. This difference reflects the intrinsic features of the Dirac-Hartree-Bogoliubov framework, where densities are obtained self-consistently by solving the Dirac equation with meson-exchange interactions and pairing correlations at the mean-field level (see Refs. [18, 30]). Such a treatment generally produces a more compact interior density due to relativistic effects and the saturation mechanism of nuclear matter. By contrast, the experimental density [29], derived from electron-scattering charge distributions and converted to matter density, tends to smooth the central peak, leading to a less pronounced core density. Beyond $r \approx 2$ fm, however, both distributions converge, as the nuclear surface dominates. Since folding-model potentials and elastic scattering cross sections are primarily sensitive to the surface region, the central-density difference is expected to have minimal impact on the present results.

Figure 2 illustrates the computed potentials at 78.85 and 420 MeV, representing the lowest and highest energies considered, respectively. For the BNP potential, only the results at 420 MeV are displayed due to its energy independence. Both potentials share a similar shape, although the SPP2 potential is shallower than the BNP potential, particularly evident at short distances ($r \leq 4$ fm). Furthermore, the SPP2 exhibits a pronounced sensitivity to energy, with its depth decreasing as the energy escalates from 78.85 to 420 MeV. At shorter distances, potentials derived from the ED density manifest deeper depths compared to those from the DHB density. However, at distances beyond 4 fm, potentials from both densities display approximately equal strength.

The accuracy of the computed potentials was evaluated by comparing the calculated elastic cross sections for $^{12}C + ^{12}C$ over the energy range of 78.85 to 420 MeV with experimental data, as shown in Figures 3 to 10. The resulting parameters of the potentials, including the volume integrals and the total

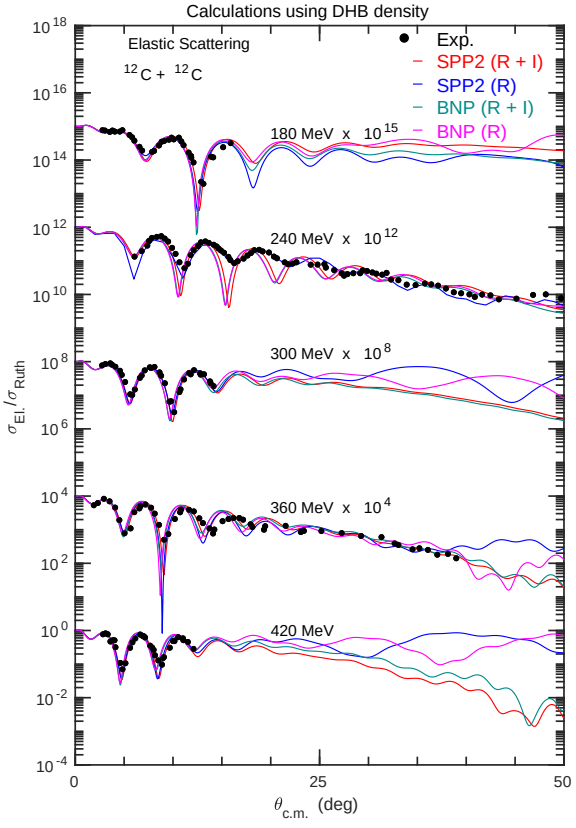

Figure 6: Same as Figure 3, but with the DHB density at 180, 240, 300, 360, and 420 MeV. Experimental data are taken from Ref. [32].

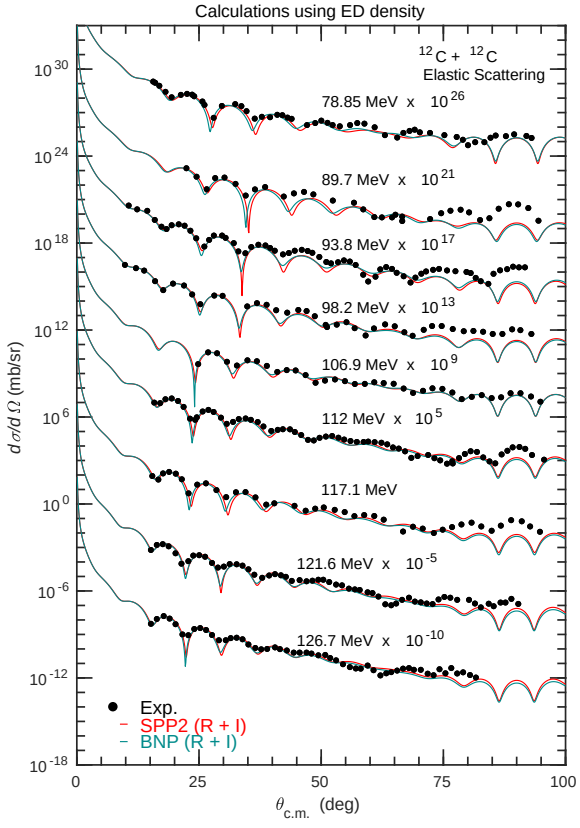

Figure 7: Ratio of elastic scattering to Rutherford cross section for $^{12}C + ^{12}C$ reaction calculated using the potentials SPP2(R+I) and BNP(R+I) with varied N_R and N_I and ED density at 78.85, 89.7, 93.8, 98.2, 106.9, 112, 117.1, 121.6 and 126.7 MeV. Experimental data are taken from Ref. [31]

reaction cross section σ_R, are detailed in Tables 1 to 3.

In this study, we explore two main approaches to ascertain the depths of various potentials SPP(R+I), SPP2(R), BNP(R+I), and BNP(R)) required for achieving complete agreement with the data (see Section 2). In the first approach, for each density distribution, we set N_R to unity and treat a set of coefficients N_I (for folding) or W_I (for Wood-Saxon) as parameters to be determined through a fit to experimental cross-section data using the standard reduced chi-square procedure. Conversely, in the second approach, we construct both the real and imaginary potentials using the double-folding model, allowing the coefficients N_R and N_I to vary and be determined from the fit to the experimental data via the Chi-square method. The fitted N_R and N_I, pertaining to the depths of the real and imaginary OPs respectively, can be regarded as measures of deviations of the potentials (SPP2 and BNP) from the scenario where N_R and N_I equal unity.

Using the first approach, we present calculated results of $^{12}C+^{12}C$ elastic scattering cross sections employing ED and DHB densities, respectively, and compare them with experimental data in Figures 3 – 4 and Figures 5 – 6. The optimal OP parameters for these calculations are listed in Tables 1 and 2 for ED and DHB, respectively. Examination of these figures reveals a similar oscillatory pattern in cross sections from all potentials at forward scattering angles, while significant differences emerge at backward scattering angles. For the ED density case, a comprehensive assessment of Figures 3 and 4 and the goodness of fit, as indicated by the χ^2/N values in Table 1, suggests that SPP2 generally outperforms BNP. Similarly, in the case of DHB, an analysis of Figures 5 and 6, along with potential parameters in Table 2, indicates that SPP2(R+I) consistently outperforms BNP(R+I) for all energies, while BNP(R) performs better than SPP2(R) at energies below 180 MeV, and vice versa at 180 MeV and above.

Additionally, employing the second approach, we present theoretical results and compare them with experimental data in Figures 7 and 8 for ED density and Figures 9 and 10 for DHB density. The parameters of the potentials for each density distribution are listed in Table 3. By treating N_R and N_I as adjustable parameters, the fit quality of the calculated results to data significantly improved compared to the first approach. Furthermore, there was a noticeable enhancement in the χ^2/N values listed in Table 3 when compared with those in Tables 1 and 2. Generally, considering the values of N_R, N_I, and χ^2/N listed in Table

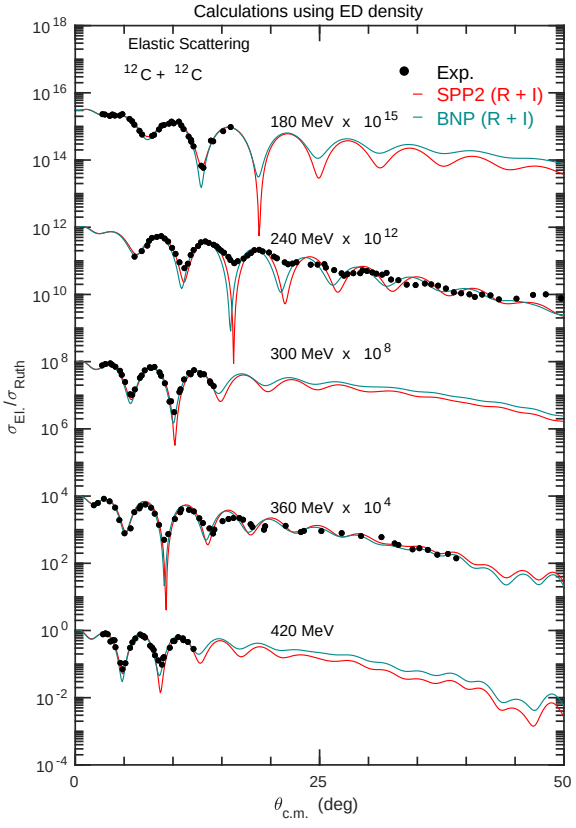

Figure 8: Same as Figure 7 but for 180, 240, 300, 360, and 420 MeV. Experimental data are taken from Ref. [32].

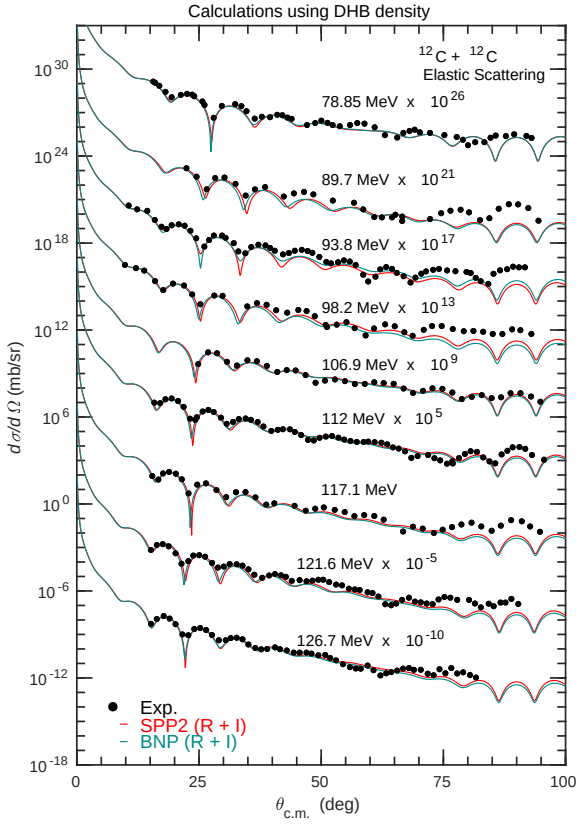

Figure 9: Same as Figure 7 but for DHB density.

3, the results obtained using the ED density describe the data better than those using DHB, and SPP2 also outperforms BNP for all energies. It is evident that in both approaches, regardless of the density used, the results are in good agreement with the experimental data.

4.2. *Volume integrals J_R and J_I*

The energy dependence of the real (J_R) and imaginary (J_I) volume integrals for the two densities is shown in Figures 11 and 12. In the first approach, J_R for SPP2 decreases with energy, while BNP remains nearly constant; in the second, both SPP2 and BNP show a decreasing trend. By contrast, J_I displays no clear systematic energy dependence in either approach. For both densities, however, J_I is consistently larger for SPP(R+I) and BNP(I+R) than for SPP2(R) and BNP(R), and the values obtained with ED are slightly higher than with DHB.

These results have clear physical implications. The decrease of J_R with energy (except for BNP in the first approach) reflects the dispersion relation between real and imaginary potentials and the weakening of refractive effects at higher energies. The lack of systematic behavior in J_I is consistent with global optical-model trends, though its larger values when both real and imaginary components are included indicate stronger absorption. The slightly higher J_I from ED compared to DHB further suggests that the experimental density, being less compact, enhances coupling to non-elastic channels. Overall, the J_R trends support the robustness of the folding-model description, while the variations in J_I highlight its sensitivity to both the interaction and the density input.

4.3. *Reaction cross section σ_R*

In addition to the parameters of the potentials, the reaction cross section σ_R is listed in Tables 1 to 3. It is defined as [33]

$$\sigma_R = \frac{\pi}{k}\sum_L (2L+1)(1-|S_L|^2), \tag{11}$$

where the wave number $k = (2\mu E_{c.m.}/\hbar^2)^{1/2}$, μ is the reduced mass $E_{c.m.}$ is the energy in the center-of-mass frame, and S_L is the complex scattering matrix for the L-th partial wave, and it is related to the real reflection coefficients a_L and the scattering phase shifts δ_L by $S_L = a_L e^{2i\delta_L}$.

To further investigate the differences between the velocity-dependent SPP2(R+I) and velocity-independent BNP (R+I) potentials, using the fit parameters in Table 3, we show the plot of the magnitudes of partial-wave scattering (S–matrix) elements $|S_L|$ versus the angular momentum L for all energies in Figure 13.

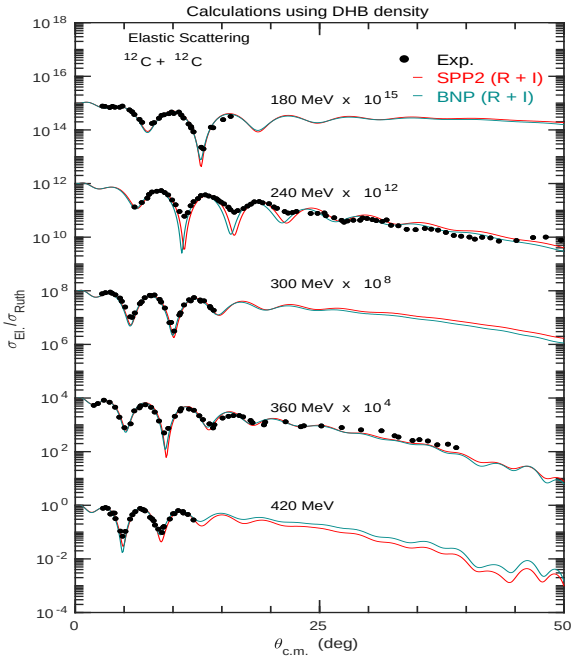

Figure 10: Same as Figure 8 but for DHB density.

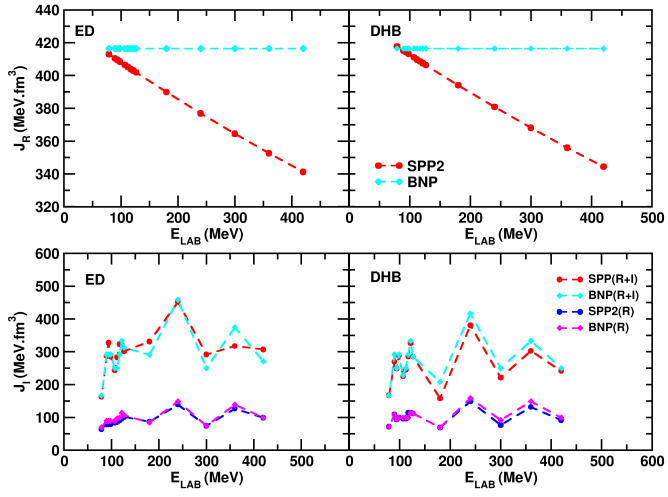

Figure 11: Energy dependence of the volume integrals J_{R} and J_{I} for the potentials SPP2(R+I), SPP2(R), BNP(R+I), and BNP(R) with fixed $N_R = 1$ and varied N_I, using ED and DHB densities.

In this figure, we observe that the value of $|\,S_L\,|$ is approximately 0 at small values of L, gradually escalating as L increases, eventually approaching unity. However, the span of L values needed for $|\,S_L\,|$ to rise from 0 to 1 expands with higher incident energy, and this span remains nearly consistent across all considered potentials. Furthermore, the sensitivity of $|\,S_L\,|$ to densities under the same potentials is notable. Specifically, the range of L values required for $|\,S_L\,|$ to progress from 0 to 1 is greater for ED density compared to DHB density. The

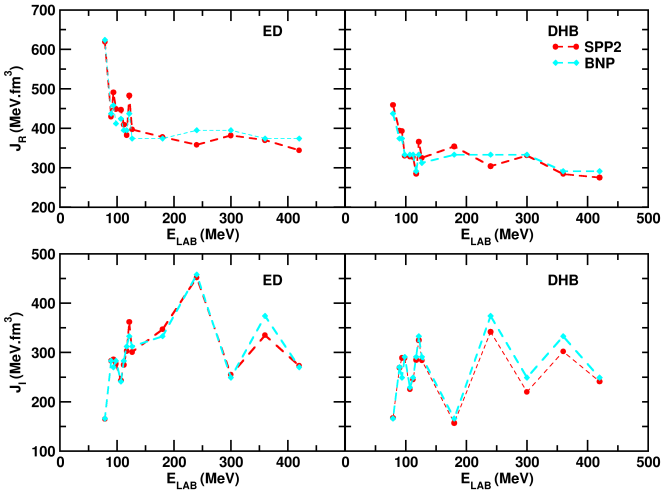

Figure 12: Energy dependence of the volume integrals J_{R} and J_{I} for the potentials SPP2(R+I) and BNP(R+I) with varied N_R and N_I, using ED and DHB densities.

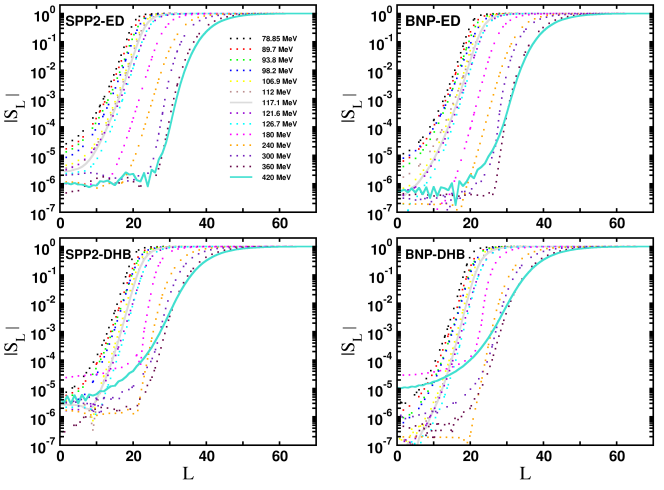

Figure 13: Scattering matrix element $|\,S_L\,|$ versus the angular momentum L for the for ^{12}C+^{12}C at E_{Lab} = 78.85,89.7, 93.8, 98.2, 106.9, 112, 117.1, 121.6, 126.7, 180, 240, 300, 360 and 420 MeV.

value of $|\,S_L\,|$ indicates the level of absorption. For example, $|\,S_L\,| = 1$ for elastic scattering means no absorption. Furthermore, it has been suggested that total absorption happens when the transmission coefficient $(1-|\,S_L\,|^2)$ equals zero [34]. Also, as can be seen in Figure 13, the dependency of $|\,S_L\,|$ on the angular momentum L shown by the SPP2 is somewhat similar to that shown by the BNP potential, and this is also true for ED and DHB densities. To further investigate the sensitivity of the reaction cross section σ_R to the different potentials and density distribution, we calculate the differentiation of the scattering matrix elements $|\,S_L\,|$ with respect to L,

$$\frac{d\,|\,S_L\,|}{dL} = \frac{|\,S_{L+1}\,| - |\,S_{L-1}\,|}{(L+1)-(L-1)} = \frac{|\,S_{L+1}\,| - |\,S_{L-1}\,|}{2}, \quad (12)$$

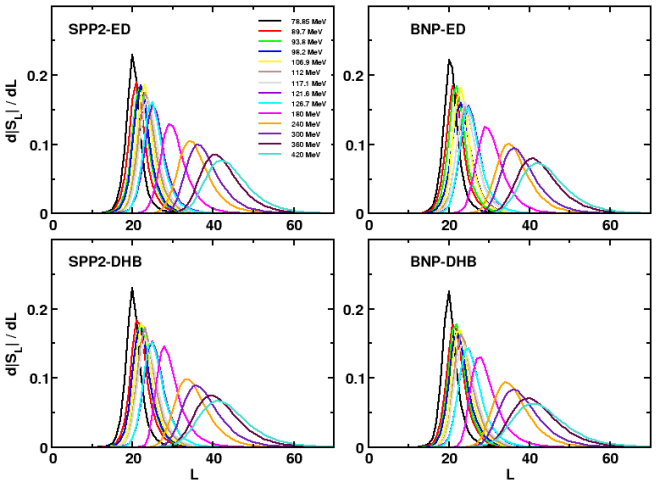

Figure 14: Derivative of the s-matrix element $\frac{d|S_L|}{dL}$ versus the angular momentum for ^{12}C+^{12}C at $E_{\rm Lab}$ = 78.85,89.7, 93.8, 98.2, 106.9, 112, 117.1, 121.6, 126.7, 180, 240, 300, 360 and 420 MeV.

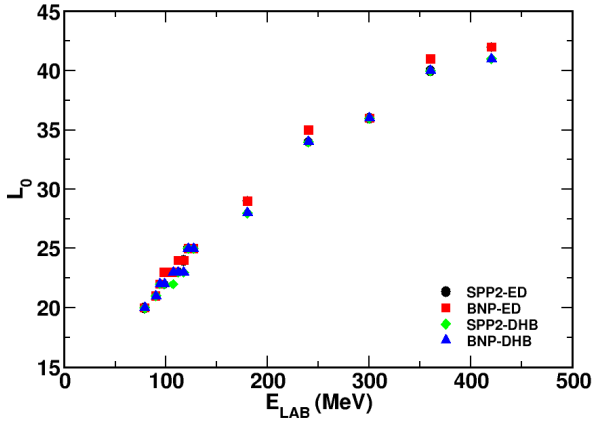

Figure 15: Energy evolution of the centroid L_o of the curve $\frac{d|S_L|}{dL}$ for ^{12}C+^{12}C reaction.

and the relationship between the differentiation curve and the angular momentum L for the different potentials and densities is shown in Figure 14. As can be seen in this figure, the shape of $\frac{d|S_L|}{dL}$ is very close to a Gaussian shape,

$$\frac{d\mid S_L\mid}{dL} \approx \text{constant} \times \exp\left(-\left(\frac{L-L_o}{\Delta L}\right)^2\right), \qquad (13)$$

where L_o represents the centroid of the curve (which corresponds to the value of L at maximum $\frac{d|S_L|}{dL}$) and ΔL represents the width of the curve. Figure 15 shows the plot of L_o versus the incident energy for all potentials with their corresponding density. It can be seen from the figure that L_o generally increases with increasing energy, and the value of L_o for the BNP potential calculated with the DHB density (denoted as BNP-DHB) is consistently higher than those of SPP2-ED, SPP2-DHB, and BNP-ED, which give almost the same value of L_o at each energy.

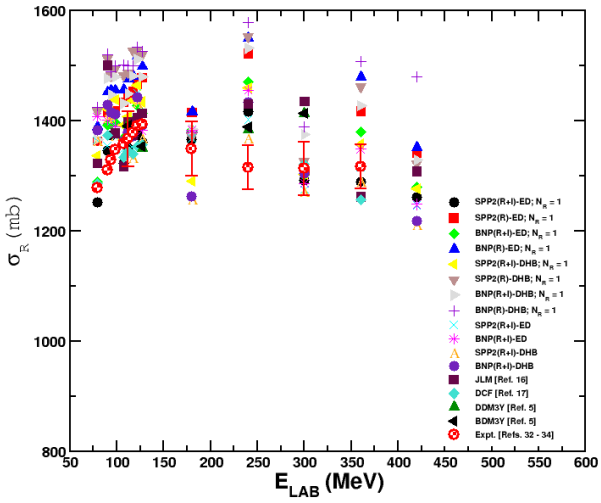

Figure 16: Energy dependence of the reaction cross section $\sigma_{\rm R}$ for the ^{12}C+^{12}C system, comparing the present results with previous works [5, 6, 16, 17] and experimental data [32, 35, 36].

The reaction cross sections, σ_R, obtained in this study for the various potentials are presented in the second-to-last columns of Tables 1, 2, and 3. Figure 16 shows the energy dependence of σ_R from the present calculations, compared with results of earlier studies based on the DDM3Y and BDM3Y interactions [5], the JLM potential [16], and the DFC potential [17], as well as with available experimental data [32, 35, 36]. From Tables 1, 2, and 3, together with Figure 16, several key observations can be made. First, the σ_R values obtained with the velocity-independent BNP interaction are systematically higher than those from the velocity-dependent SPP2 interaction. Second, calculations with the DHB density consistently give larger σ_R values than those with the ED density. However, the differences between results from the different potentials or between the two densities are generally within 5%. Finally, the present σ_R values are broadly consistent with those obtained in previous works employing the DDM3Y, BDM3Y [5], JLM [16], and DFC [17] interactions.

Figure 16 further shows that at low and intermediate energies (78.9–126.7 MeV), all theoretical models reproduce the overall energy dependence of the experimental data, though most systematically overestimate the cross sections. For instance, while the measured values lie between 1277 and 1393 mb in this region, the theoretical predictions extend up to 1527 mb. Among the parametrizations, SPP2(R+1)-ED; N_R = 1 and BNP(R+I)-ED; N_R = 1 (i.e., SPP2 and BNP using ED density with N_R = 1) provide the closest agreement with experiment, whereas corresponding parametrizations with the DHB density (SPP2(R+1)-DHB; N_R = 1 and BNP(R+I)-DHB; N_R = 1) tend to overpredict. This systematic difference primarily reflects the sensitivity of σ_R to the imaginary potential parameters, which determine the strength of absorption into non-elastic channels.

Stronger absorption, reflected in larger imaginary volume integrals, naturally enhances the calculated σ_R, as clearly seen in the BNP4 and SPP4 cases.

At higher energies (180–420 MeV), the agreement between theory and experiment improves significantly. In particular, at 300 and 360 MeV, the calculated cross sections for most parametrizations (1270–1380 mb) are nearly identical to the experimental values (1313–1316 mb within uncertainties). This indicates that at higher bombarding energies, the sensitivity of σ_R to the fine details of the optical potential diminishes, with all parametrizations converging toward a common description dominated by geometric effects. Nonetheless, slight overpredictions remain in some cases (e.g., SPP2(R)-DHB and BNP(R)-DHB), suggesting that the absorption strengths in these parametrizations may still be somewhat too large.

4.4. The χ^2/N values

The quality of the fits obtained with the SPP2 potentials can be directly compared with earlier folding-model calculations using the DDM3Y/BDM3Y interaction [5] and the density-folding cluster (DFC) model [17], as shown in the last columns of Tables 1 – 3. Across the near–barrier energies, the SPP2 parametrizations generally provide lower or at least comparable chi-square values relative to the earlier models. In particular, the SPP2 framework yields substantial improvements at 78.9 and 89.7 MeV, where the χ^2/N values are reduced by nearly a factor of two to three compared with DDM3Y/BDM3Y. Further, at 112.0 and 126.7 MeV, the SPP2 results outperform both DDM3Y/BDM3Y and DFC, achieving the most accurate description of the scattering data in this energy region.

At higher energies, the advantage of the SPP2 parametrizations becomes even more striking. At 240 MeV, the SPP2 results improve upon the DFC description, while at 300 MeV they yield χ^2/N values almost an order of magnitude smaller than those of both DDM3Y/BDM3Y and DFC. Even at 360 MeV, the SPP2 values remain competitive, matching or surpassing the earlier folding-model calculations.

Taken together, the systematic reduction in χ^2/N values over a broad range of energies demonstrates that the SPP2 approach provides a more consistent and accurate description of the ^{12}C+^{12}C elastic scattering data than the conventional folding models. These results reinforce the reliability of the SPP2 framework as a robust tool for heavy–ion scattering analyses.

5. Conclusion

In this study, we have investigated the elastic scattering cross sections for ^{12}C + ^{12}C over a wide range of incident energies from 78.85 to 420 MeV. The analysis was conducted utilizing the velocity-dependent Sao Paulo Potential version 2 (SPP2) and the velocity-independent Brazilian Nuclear Potential (BNP) within the framework of the optical-model-based double folding (DF) model. Two different matter density distributions for ^{12}C were considered: the experimental density (ED) and the theoretical density derived from the Dirac-Hartree-Bogoliubov (DHB) model.

Comparative analysis of the density distributions revealed distinct characteristics, with the DHB density exhibiting higher values at the nucleus's center and the ED density dominating at the surface. However, beyond r = 2 fm, both distributions exhibit a similar shape and density value.

The computed potentials indicated that while both SPP2 and BNP shared similar shapes, SPP2 exhibited energy sensitivity, with its depth decreasing as the incident energy increased. Furthermore, potentials derived from the ED density generally displayed deeper depths compared to those from the DHB density, particularly at shorter distances.

Evaluation of the accuracy of the computed potentials through comparison with experimental data revealed that, overall, SPP2 outperformed BNP in describing the elastic scattering cross sections for both ED and DHB densities. This superiority was evident across all energies considered.

Two main approaches were explored to ascertain the depths of various potentials required for agreement with the data. The first approach involved setting certain coefficients as parameters to be determined via a fit to experimental cross-section data, while the second approach constructed both real and imaginary potentials using the double-folding model, allowing for variations in these coefficients.

Analysis of the energy dependence of the real and imaginary volume integrals (J_R and J_I) indicated distinct behaviors for SPP2 and BNP, with J_R decreasing with increasing energy for SPP2 and remaining constant for BNP, when the real potential in not renormalised and the imaginary normalization constant or WS depth is varied. However, the two parameters (J_R and J_I) show variation with energy when the depths of both the real and imaginary potentials are varied. Additionally, J_I values were consistently higher for SPP(R+I) and BNP(I+R) compared to SPP2(R) and BNP(R), with slightly higher values for the ED density compared to DHB.

Further investigation into the reaction cross section σ_R revealed that while differences existed between the various potentials and density distributions, these discrepancies were relatively small, with differences not exceeding 5%. Additionally, the obtained σ_R values were consistent with those from previous studies based on different potentials, as well as with experimental data.

The χ^2/N systematics show that the SPP2 framework provides a more accurate and consistent description of ^{12}C+^{12}C elastic scattering than the DDM3Y/BDM3Y [5] and DFC [17] models, with particularly significant improvements at both near–barrier and higher energies.

In conclusion, the results of this study demonstrate the efficacy of the SPP2 potential, particularly when combined with the ED density, in accurately describing the elastic scattering cross sections for ^{12}C + ^{12}C over a broad range of energies. The findings contribute to a deeper understanding of nuclear interactions and provide valuable insights for future research in this field.

Data availability

The data supporting the findings of this study are available from the corresponding author upon reasonable request.

References

[1] G. R. Satchler & W. G. Love, "Folding model potentials from realistic interactions for heavy-ion scattering", Physics Reports **55** (1979) 183. https://doi.org/10.1016/0370-1573(79)90081-4.

[2] A. M. Kobos, B. A. Brown, P. E. Hodgson, G. R. Satchler & A. Budxanowski, "Folding model anallysis of α–particle elastic scattering with a semirealistic density–dependent effective interaction", Nuclear Physics A **384** (1982) 65. https://doi.org/10.1016/0375-9474(82)90305-0.

[3] A. M. Kobos, B. A. Brown, R. Lindsay & G. R. Satchler, "Optical potentials for heavy-ion elastic scattering", Nuclear Physics A **425** (1984) 205. https://doi.org/10.1016/0375-9474(84)90073-3.

[4] M. E. Farid & G. R. Satchler, "A density–dependent interaction in the folding model for heavy–ion potentials", Nuclear Physics A **438** (1985) 525. https://doi.org/10.1016/0375-9474(85)90391-4.

[5] D. T. Khoa, W. von Oertzen & H. G. Bohlen, "Double–folding model for heavy-ion optical potential: revised and applied to study ^{12}C and ^{16}O elastic scattering ", Physical Review C **49** (1994) 1652. https://doi.org/10.1103/PhysRevC.49.1652.

[6] D. T. Khoa, W. V. Oertzen, H. G. Bohlen, G. Bartnitzky, H. Clement, Y. Sugiyama, B. Gebauer, A. N. Ostrowski, T. Wilpert, M. Wilpert & C. Langner, "Equation of state for cold nuclear matter from refractive ^{16}O+^{16}O elastic scattering", Physical Review Letters **74** (1995) 34. https://doi.org/10.1103/PhysRevLett.74.34.

[7] S. Hossain, M. N. A. Abdullah, K. M. Hasan, M. Asaduzzaman, M. A. R. Akanda, S. K. Das, A. S. B. Tariq, M. A. Uddin, A. K. Basak, S. Ali & F. B. Malik, "Shallow folding potential for ^{16}O + ^{12}C elastic scattering ", Physics Letters B **636** (2006) 248. https://doi.org/10.1016/j.physletb.2006.03.071.

[8] D. T. Khoa, N. H. Phuc, D. T. Loan & B. M. Loc, "Nuclear mean field and double-folding model of the nucleus–nucleus optical potential ", Physical Review C **94** (2016) 034612. http://link.aps.org/doi/10.1103/PhysRevC.94.

[9] M. E. Brandan & G. R. Satchler, "The interaction between light heavy-ions and what it tells us", Physics Reports **285** (1997) 143. https://doi.org/10.1016/S0370-1573(96)00048-8.

[10] A. J. Cole, W. D. M. Rae, M. E. Brandan, A. Dacal, B. G. Harvey, R. Legrain, M. J. Murphy & R. G. Stokstad, "^{12}C+^{12}C reaction cross section between 70 and 290 MeV obtained from elastic scattering", Physical Review Letters **47** (1981) 1705. https://doi.org/10.1103/PhysRevLett.47.1705.

[11] H. G. Bohlen, X. S. Chen, J. G. Cramer, P. Frobrich, B. Gebauer, H. Lettau, A. Miczaika, W. von Oertzen, R. Ulrich & T. Wilpert, "Refractive scattering and the nuclear rainbow in the interaction of ^{12,13}C with ^{12}C at 20 MeV/N ", Zeitschrift für Physik A Atoms and Nuclei **322** (1985) 241. https://doi.org/10.1007/BF01411889.

[12] E. Stiliaris, H. G. Bohlen, P. Frobrich, B. Gebaur, D. Kolbert, W. von Oertzen, M. Wilpert & Th. Wilpert, "Nuclear rainbow structures in the elastic scattering of ^{16}O on ^{16}O at E_L = 350 MeV",Physics Letters B **223** (1989) 291. https://doi.org/10.1016/0370-2693(89)91604-3.

[13] G. Bertsch, J. Borysowicz, H. McManus & W. G. Love, "Interactions for inelastic scattering derived form realistic potentials", Nuclear Physics A **284** (1977) 399. https://doi.org/10.1016/0375-9474(77)90392-X.

[14] D. T. Khoa, N. H. Phuc, D. T. Loan & B. H. Loc, "Nuclear mean field and double–folding model of the nucleus–nucleus optical potential", Physical Review C **94** (2016) 034612. https://doi.org/10.1103/PhysRevC.94.034612.

[15] N. Rowley, H. Doubre & C. Marty, "Low partial waves in ^{12}C+^{12}C elastic scattering", Physics Letter B **69** (1977) 147. https://doi.org/10.1016/0370-2693(77)90630-X.

[16] Z.M.M. Mahmoud & M.A. Hassanien, "Analysis of ^{12}C+^{12}C elastic scattering for energy between 70 and 1440 MeV ", Physics of Atomic Nuclei **82** (2019) 599. https://doi.org/10.1134/S1063778819060103.

[17] M. A. Hassanain, A. A. Ibraheem & M. E. Farid, "Double folding cluster potential for ^{12}C+^{12}C elastic scattering", Physical Review C **77** (2008) 034601. https://doi.org/10.1103/PhysRevC.77.034601

[18] L. C. Chamon, B. V. Carlson & L. R. Gasques, "São Paulo potential version 2 (SPP2) and Brazilian nuclear potential (BNP) ", Computer Physics Communications **267** (2021) 108061. https://doi.org/10.1016/j.cpc.2021.108061.

[19] A. A. Ibraheem & H. Al-Amri, "Analysis of ^{4,6,8}He+^{208}Pb elastic scattering at E = 22 MeV using various potentials", Revista Mexicana de Fisica 68051201 (2022) 1. https://doi.org/10.31349/RevMexFis.68.051201.

[20] Sh. Hamada & A. A. Ibraheem, "Reanalysis of ^{6}Li+^{90}Zr angular distributions using different nuclear potentials", Journal of Taibah University for Science **16** (2022) 163. https://doi.org/10.1080/16583655.2022.2036428.

[21] U. Umbelino, R. Lichtenthäler, O.C. Santos, K. C. Pires, A. S. Serra, V. Scarduelli, A. L. de Lara, E. O. Zevallos, J. C. Zamora, A. Lepine–Szily, J. M. B. Shorto, M. Assunifmmode & V. A. B. Zagatto, "Quasielastic scattering of light radioactive and stable projectiles on ^{9}Be" Physical Review C **106** (2022) 054602. https://doi.org/10.1103/PhysRevC.106.054602.

[22] S. D. Olorunfunmi & A. Bahini, "Reanalysis of ^{10}B+^{120}Sn Elastic Scattering Cross Section Using São Paulo Potential Version 2 and Brazilian Nuclear Potential", Brazilan Journal of Physics **52** (2022) 11. https://doi.org/10.1007/s13538-021-01018-y.

[23] S. D. Olorunfunmi, S. A. Adeojo & A. Bahini, "Investigation of elastic scattering angular distributions of ^{12,13}C + ^{90,91,92,94,96}Zr: a comparative analysis of different optical model potentials", Indian Journal of Physics **98** (2024) 7. https://doi.org/10.1007/s12648-023-03025-y

[24] A. H. Amer, Z. M. M. Mahmoud & Yu. E. Penionzhkevich, "Double folding analysis of α+^{12}C elastic scattering using different effective interactions", Nuclear Physics A (2022) 1020. https://doi.org/10.1016/j.nuclphysa.2022.122398.

[25] M. N. El-Hammamy, A. A. Ibraheem, M. E. Farid, E. F. Elshamy & S. Hamada, "Comprehensive examination of the elastic scattering angular distributions of ^{10}C+^{4}He, ^{27}Al, ^{58}Ni and ^{208}Pb using various potentials", Revista Mexicana de Fisica **69** (2023) 031201. https://doi.org/10.31349/RevMexFis.69.031201.

[26] M. Nassurlla, N. Burtebayev, S. B. Sakuta, Sh. Hamada, S. V. Artemov, K. Rusek, N. Marzhan, N. Amangeldi, B. Mauyey, G. Yergaliuly, F. Ergashev, A. Sabidolda, R. Khojayev, Y. B. Mukanov, E. Piasecki & Awad A. Ibraheem, "Scattering of ^{10}B ions on ^{11}B nuclei at an energy of 41.3 MeV", The European Physical Journal A **60** (2024) 30. https://doi.org/10.1140/epja/s10050-023-01220-3.

[27] L. C. Chamon, L. R. Gasques & B. V. Carlson, "Velocity–dependent model for the α–α interaction in the context of the double–folding potential", Physical Review C **101** (2020) 034603. https://doi.org/10.1103/PhysRevC.101.034603.

[28] L. C. Chamon, L. R. Gasques & B. V. Carlson, "Approximate treatment of relativistic effects in the low-energy α+α scattering", Physical Review C **84** (2011) 044607. https://doi.org/10.1103/PhysRevC.84.044607.

[29] H. De Vries, C.W. De Jager & C. De Vries, "Nuclear charge-density-distribution parameters from elastic electron scattering" Atomic Data and Nuclear Data Tables **36** (1987) 495. https://doi.org/10.1016/0092-640X(87)90013-1

[30] B.V. Carlson & D. Hirata, "Dirac-Hartree-Fock-Bogoliubov approximation for finite nuclei", Physical Review C **62** (2000) 054310. https://doi.org/10.1103/PhysRevC.62.054310

[31] R. G. Stokstad, R. M. Wieland, G. R. Satchler, C. B. Fulmer, D. C. Hensley, S. Raman, L. D. Rickertsen, A. H. Snell & P. M. Stelson, "Elastic and inelastic scattering of ^{12}C by ^{12}C from $E_{\mathrm{c.m.}}$ = 35 – 63 MeV", Physical Review C **20** (1979) 655. https://link.aps.org/doi/10.1103/PhysRevC.20.655.

[32] C. C. Sahm, T. Murakarni, J. G. Cramer, A. J. Lazzarini, D. D. Leach, D. R. Tieger, R. A. Loveman, W. G. Lynch, M. B. Tsang & J. Van der Plicht, "Total reaction cross section for ^{12}C on ^{12}C, ^{40}Ca, ^{90}Zr, and ^{208}Pb between 10 and 35 MeV/nucleon", Physical Review C **34** (1986) 2165. https://link.aps.org/doi/10.1103/PhysRevC.34.2165.

[33] P. Mohr, Z. Fülöp, G. Gyürky, G. G. Kiss & T. Szücs, "Successful prediction of total α–induced reaction cross sections at astrophysically relevant sub-Coulomb energies using a novel approach", Physical Review Letters **124** (2020) 252701. https://doi.org/10.1103/PhysRevLett.124.252701.

[34] M. C. Mermaz, "Phase shift analysis of heavy-ion elastic scattering measured at intermediate energies", Zeitschrift für Physik A **321** (1985) 613 https://doi.org/10.1007/BF01432438.

[35] S. Kox, A. Gamp, C. Perrin, J. Arvieux, R. Bertholet, J. F. Bruandet, M. Buenerd, R. Cherkaoui, A. J. Cole, Y. El–Masri, N. Longequeue, J. Menet, F. Merchez & J. B.Viano, "Trends of total reaction cross sections for heavy ion collisions in the intermediate energy range", Physical Review C **36** (1987) 1687. https://link.aps.org/doi/10.1103/PhysRevC.35.1678.

[36] M. Buenerd, A. Lounis, J. Chauvin, D. Lebrun, P. Martin, G. Duhamel, J.C. Gondrand, G. Duhamel, J.C. Gondrand & P. De Saintignon, 'Elastic and inelastic scattering of carbon ions at intermidiate energies', Nuclear Physics A **424** (1984) 313. https://doi.org/10.1016/0375-9474(84)90186-6.